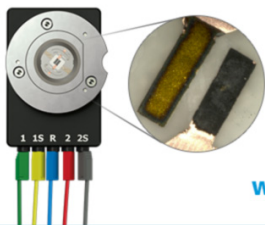


A Study of Transport Properties and Stress Analysis Using Atomistic and Macro Simulations for Lithium-Ion Batteries

To cite this article: Utsav Kumar *et al* 2014 *J. Electrochem. Soc.* **161** A1453

View the [article online](#) for updates and enhancements.

Visualize the processes inside your battery!
Discover the new ECC-Opto-10 and PAT-Cell-Opto-10 test cells!



- Battery test cells for optical characterization
- High cycling stability, advanced cell design for easy handling
- For light microscopy and Raman spectroscopy

www.el-cell.com +49 (0) 40 79012 734 sales@el-cell.com

EL-CELL[®]
electrochemical test equipment





A Study of Transport Properties and Stress Analysis Using Atomistic and Macro Simulations for Lithium-Ion Batteries

Utsav Kumar,^a Atanu K. Metya,^a N. Ramakrishnan,^b and Jayant K. Singh^{a,z}

^aDepartment of Chemical Engineering, Indian Institute of Technology Kanpur, Kanpur 208016, India

^bCentre for Study of Science Technology and Policy, Gokula, Bangalore 560054, India

Performance of a lithium-ion based rechargeable battery is investigated using coupled battery model including heat and stress models via finite element method simulations. An effort is made to elucidate the importance of using diffusivity equation, in the model, as a function of lithium-ion concentration and temperature. Diffusivity expressions for both anode and cathode material are developed using atomistic simulations. Simulation results show ~10% drop in the battery potential after 100 charge-discharge cycles. This decline in performance is attributed to the concentration gradient, heat generation and stress accumulation, substantiating the need to address these effects simultaneously. Finally, intercalation stress values due to the modified diffusivity expression are found to differ considerably with that due to the constant diffusion values used in earlier works. The findings validate the assertion that intercalation stress values depend greatly on the lithium-ion concentration based diffusivity expression.

© 2014 The Electrochemical Society. [DOI: 10.1149/2.1171409jes] All rights reserved.

Manuscript submitted March 3, 2014; revised manuscript received June 9, 2014. Published June 25, 2014.

Lithium-ion batteries are an excellent source of energy storage,¹ and can provide a high energy density. Further, they are flexible, lightweight, and have longer lifespan.² On the other hand, some of the major shortcomings are high cost, low temperature tolerance,³ cell degradation⁴ and thermal runaway.⁵ Overall, the battery performance is dependent on the nature of the electrodes, electrolytes, and the electrode-electrolyte interfaces. On the other hand, safety is related to the stability of the electrode materials and its interface with electrolyte. Hence, there have been extensive investigations^{6,7} into the battery electrodes and electrolyte materials for improving safety and performance of lithium-ion batteries. Some of the notable advances in recent years are the use of LiFePO₄ (olivine structure) as a cathode material in doped nano-sized form,⁸ improving both capacity retention during charge-discharge cycle and high discharge performance. In particular, use of free standing silicon-single wall carbon nanotube as an anode has increased the anode capacity up to 20 times compared to the conventional anode.⁹ In case of battery electrolytes, replacement of liquid electrolytes with polymer or solid electrolytes resulted in increased safety and flexibility.⁶ Further, adding certain additives improved its conductivity, which was one of the key issues with such electrolytes.⁷

Improving battery setup in terms of its performance requires analysis of overall battery behavior for different combinations of electrodes and electrolytes. Spectroscopy or diffraction techniques like nuclear magnetic resonance (NMR),¹⁰ electrochemical impedance spectroscopy (EIS)¹¹ and in situ X-ray diffraction (XRD)¹² are typically used in experiments to investigate lithium-ion battery performance. Moreover, for investigation at nano-scale, requiring high spatial resolution optical microscopy, scanning electron microscopy (SEM)¹³ and transmission electron microscopy (TEM)¹³ are used for in-depth analysis. However, requirement of high level of vacuum, constant danger of contamination and possibility of high-energy electrons interfering with battery operations limits its usability. On the other hand, modeling and simulation can emulate the battery process allowing investigation on parameters that are usually not accessible in experiments. Battery modeling has been done at different length and time scales. For example, ab-initio simulations are used to study electrode structure and lithium migration barriers;^{14,15} molecular dynamics simulations¹⁶⁻¹⁸ are used to understand the electrode-electrolyte interface physics, electrode stability and transport of lithium ions. Macroscopic model can be used to monitor overall performance, life, cost and safety of battery.¹⁹

Most of the earlier works related to modeling of battery performance and safety are based on battery model developed by Doyle et al.²⁰ Recently, few workers have appended a heat model to the battery model of Doyle et al.²⁰ to analyze the discharge performance, and

obtained heat effects and temperature dependent expression²¹⁻²³ for various transport, kinetics and mass-transfer parameters. These modified models are developed to inspect the change in temperature during charging and discharging processes, and its further effect on battery performance through temperature dependent parameters. More importantly, from safety point of view, it can be used to analyze thermal runaway condition.⁵ In addition to the inclusion of a heat model in the model of Doyle and co-workers, it was also felt important to include an intercalation stress model.^{24,25} The decline in the battery performance is predominantly attributed to the capacity fade problem as a consequence of intercalation stress. It has also been reported that prolong accumulation of stress may even lead to electrode cracking.²⁶ Apart from insertion/extraction of lithium-ion, structural failures also arise due to heat generation and concentration gradient developed during charge-discharge cycles at different operating conditions. These findings demand the need to simultaneously monitor the effect of predominant parameters on the performance of lithium-ion batteries.

Stress generated in battery is classified typically into two types: mechanical and non-mechanical. This paper focuses on non-mechanical part of stress, which is further classified into two kinds viz., intercalation and thermal. Among these stress components, diffusion induced stress or intercalation stress have been studied more extensively.^{24,25,27,28} Zhang et al.^{24,25} developed a mathematical model for calculating intercalation-induced stress, and subsequently appended a heat model to it. Among several factors affecting outcome of stress in lithium-ion battery, diffusion of lithium-ions in electrode particles plays a vital role. Lithium-ion diffusivity expression used in earlier intercalation stress model was mainly a function of temperature; whereas, electrode diffusivity also depends on lithium-ion concentration. There is not much work done that has incorporated lithium-ion diffusivity variation with lithium-ion concentration for the study of battery performance. Chen and Verbrugge²⁹⁻³² have studied the variation of diffusion induced stress with respect to lithium-ion concentration, electrode material and electrode geometry; however, there is no specific interlink of electrode diffusivity expression with lithium-ion concentration, and its effect on intercalation stress. The understanding of ionic mechanisms in solid phases and determination of diffusivity variation with lithium-ion concentration and temperature is extremely important for an efficient battery design. There have been only few studies on the diffusion characteristics of lithium-ion in battery anode and cathode materials. For example, first-principles calculation has been used to study lithium-ion diffusion in carbon anodes.^{15,33,34} The diffusivity values for carbon anodes have also been evaluated in experiments.³⁵⁻³⁷ Similarly, ab-initio calculations have been used for finding diffusivity of lithium-ion in LiMn₂O₄ (cathode material).³⁸ In addition, classical molecular dynamics (MD) have also been used to study the lithium-ion diffusivity in LiMn₂O₄.¹⁶⁻¹⁸

This paper aims to couple micro and macro scale model to address the questions raised in the above section. First, a relation

^zE-mail: jayantks@iitk.ac.in

between lithium-ion diffusivity with temperature and electrode lithium-ion concentration is developed using MD simulations, as a part of micro modeling. It elucidates the combined effect of lithium-ion concentration and battery temperature on the lithium-ion diffusivity in electrodes, and further on the intercalation stress in anode and cathode materials. In addition, a pseudo 2D battery model coupled with a heat model and intercalation stress model are combined along with the developed electrode diffusivity expression to perform an in-depth study. Overall, a finite element analysis (FEA) of macro model is performed to evaluate the stress and temperature during battery charge-discharge cycles. The obtained simulation results explicitly explain correlation of concentration gradient, accumulation of stress, and heat generation, and are associated with the decline in battery performance. In the end, in order to reflect the importance of lithium-ion concentration on the diffusivity values, the intercalation stress values predicted using the modified electrode diffusivity expression are compared with the diffusivity values given in Doyle et al.²⁰

Model and Methodology

Atomistic model.—The diffusion coefficients are calculated using molecular dynamics simulations for both anode and cathode as described in following section.

Anode (LiC₆).—The graphite structure of dimensions 59.65 × 44.28 × 26.8 Å containing 8064 carbon atoms in eight graphene layers is used in this study. The Adaptive Intermolecular Reactive Empirical Bond Order (AIREBO)³⁹ potential is used for the graphite material. The AIREBO potential is defined by a sum over pair wise interaction, including covalent bonding (REBO) interaction, LJ terms, and torsion interactions and is given below:

$$E = \frac{1}{2} \sum_i \sum_{i \neq j} \left[E_{ij}^{REBO} + E_{ij}^{LJ} + \sum_{k \neq i} \sum_{l \neq i, j, k} E_{ijkl}^{tors} \right] \quad [1]$$

The lithium ions are placed randomly within the graphite layers. Force-field parameters for intermolecular and Columbic interactions for lithium-ion are taken from Wander and Shuford.⁴⁰ Lorentz-Berthelot combining rules are employed for the cross interactions.

Cathode (Li_xMn₂O₄).—Simulation is carried out in a cubic system of dimension 33.0 Å. The simulation box consists of 512 Li, 512 Mn (III), 512 Mn (IV) and 2048 O atoms arranged in the fd3m lattice, with a lattice parameter of 8.25 Å extended to 4 × 4 × 4 cube. The potential model employed for the cathode material is given by Eq. 2:

$$V_{ij} = -\frac{Z_i Z_j e^2}{r_{ij}} + A_{ij} \exp\left(\frac{-r_{ij}}{\rho_{ij}}\right) - \frac{C_{ij}}{r_{ij}^6} \quad [2]$$

All the interaction parameters are taken from Tachibana et al.⁴¹ Atomic coordinates of LiMn₂O₄ are adopted from Gatheshki et al.⁴² Electrostatic interactions are calculated using Ewald summation technique.

The diffusion coefficient (*D*) is calculated using the Einstein relation:

$$D = \frac{1}{6} \lim_{t \rightarrow \infty} \frac{d}{dt} \langle [r_i(t + t_0) - r_i(t_0)]^2 \rangle \quad [3]$$

In order to calculate diffusivity expression as a function of electrode's lithium-ion concentration and temperature, Arrhenius formula is used as shown in Eq. 4. The prefactor *D*_{0,*i*} depends on the lithium-ion concentration at a constant temperature.²³ We have used the modified diffusivity expression (Eq. 4) in the macro model as described in a later section.

$$D_i = D_{0,i} \exp\left(\frac{E}{R} \left(\frac{1}{T_{ref}} - \frac{1}{T}\right)\right) \quad [4]$$

Macro model.—The electro-thermal model assumed in this paper is based on the pseudo two-dimensional model developed earlier by Doyle et al.²⁰ Figure 1 shows a schematic representation of the

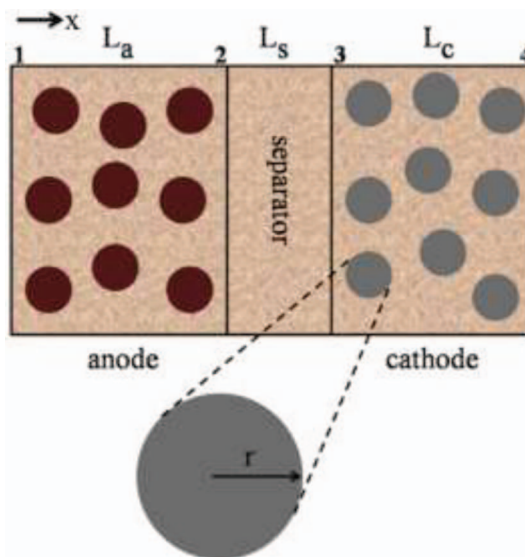


Figure 1. Schematic representation of lithium-ion battery model (*L_a*, *L_s* and *L_c* represent length of anode, separator and cathode respectively).

system assumed in this paper. In this work, ethylene carbonate and dimethyl carbonate (EC/DMC) in the ratio 2:1 is considered as the electrolyte. The positive and negative electrodes, considered to be made up of LiMn₂O₄ and LiC₆ materials, respectively. Overall, there are two inner boundaries, anode/separator surface (boundary 2) and cathode/separator surface (boundary 3) and two external boundaries (boundary 1 and 4) as shown in Fig. 1. The electrodes are considered to be porous in nature. Active materials in electrodes are assumed to be spherical in shape. We have ignored temperature gradient, inside the particle, and side reactions, if any.

In this work, the lithium-ion battery is represented by a 1D model, and active materials (electrode solid particles) are represented by a 2D model. Governing equations required for modeling lithium-ion battery are described in the following section.

Charge balance.—Charge balance equation, for electrode, is represented by Ohmic drop, and expressed as follows:

$$i_s = -\sigma_{s,eff} \nabla \phi_s \quad [5]$$

where, *i*, *σ*_{eff}, and *φ* represent current density (Am⁻²), effective conductivity and potential, respectively. *φ* is zero at boundary 1 (Eq. 6). The subscript *s* stands for electrode.

$$\phi_s|_{x=0} = 0 \quad [6]$$

At boundaries 2 and 3 (see Figure 1), charge flux is negligible i.e.,

$$-\sigma_{s,eff} \nabla \phi_s|_{x=L_a} = 0; \quad -\sigma_{s,eff} \nabla \phi_s|_{x=L_a+L_s} = 0 \quad [7]$$

The charge flux is set to the average current density at boundary 4:

$$-\sigma_{s,eff} \nabla \phi_s|_{L_a+L_s+L_c} = -I_{app} \quad [8]$$

The average charge flux is set to charge-discharge current density pulse of amplitude (*I*_{app}) 17.5 Am⁻² (see Eq. 8) with a time period of 1600 s.

Charge balance for the electrolyte is expressed as

$$i_l = -\sigma_{l,eff} \nabla \phi_l + \frac{2\sigma_{l,eff} RT}{F} \left(1 + \frac{\partial \ln f}{\partial \ln c_l}\right) (1 - t_+) \nabla \ln c_l, \quad [9]$$

where, *R*, *T*, *F*, *f*, *t*₊, and *c* represent universal gas constant, temperature, Faraday's constant, mean molar activity coefficient of the salt, transport number and concentration of lithium-ions, respectively (subscript *l* stands for electrolyte). Here, the first term of the expression simply represents Ohmic drop as in Eq. 5, and the second term describes the dependence on molar activity coefficient and concentration

gradient that makes it as a function of both concentration and temperature. This effect is included when concentrated solution theory for electrolyte is considered instead of the dilute solution theory.⁴³ In the present study, the term $\partial \ln f / \partial \ln c_l$ in Eq. 9 is assumed to be zero.

The charge flux is assumed to be continuous at the interior boundary points (2 and 3), whereas current is set to zero (Eq. 10) at the external boundary points (1 and 4). The extra term in the charge equation accommodates the concentration gradient present in the electrolyte.

$$i_l = 0. \quad [10]$$

Mass balance.—A modified Fickian diffusion is used to accommodate the effect of stress on electrode particles as expressed in Eqs. 11 and 12. A 2D model as described before in Fig. 1 represents an electrode particle. Further, concentration of lithium-ions present at the surface of electrode particle is coupled with the 1D model.

$$\frac{\partial c_s}{\partial t} = \nabla \cdot \left(D_s \left(\nabla c_s - \frac{\Omega c_s}{RT} \nabla \tau_h \right) \right), \quad [11]$$

$$\tau_h = (\tau_r + 2\tau_t), \quad [12]$$

where, D , Ω , and τ represent diffusivity constant, partial molar volume and stress, respectively. Subscripts h , r , and t stand for hydrostatic, radial and tangential components, respectively.

At external boundary, flux value (j) is constant and is related to the current density (i_{loc}) as shown in Eq. 13.

$$j = - \left(D_s \left(\nabla c_s - \frac{\Omega c_s}{RT} \nabla \tau_h \right) \right) = \frac{1.5 i_{loc}}{F}. \quad [13]$$

In this paper, the spherical electrode model is represented as a circle in 2D. A 2D circle when extended to 3D forms a cylinder with surface area/volume ratio of $2/R$. However, electrode particles are modeled as spheres, where surface area/volume ratio is $3/R$. Thus, for the same value of flux, a sphere would receive 1.5 times more lithium-ions as compared to a cylinder i.e., a factor of 1.5 is added to make the flux consistent with the assumed electrode structure.

The governing equation, for the electrolyte region, depicting mass balance deduced by concentrated solution theory⁴³ is given below:

$$\varepsilon_l \frac{\partial c_l}{\partial t} = D \frac{\partial^2 c_l}{\partial x^2} + a \left(1 - t_+^0 \right) i_{loc} \quad [14]$$

where, a is the specific interfacial area and ε_l is the porosity of electrolyte. The flux at external boundaries (1 and 4) is set to zero, and for internal boundaries (2 and 3) species flux is taken to be continuous.

Electrochemical kinetics.—The local current is evaluated based on the Butler-Volmer equation (Eq. 15):

$$i_{loc} = i_0 \left(\exp \left(\frac{\alpha_a F \eta}{RT} \right) - \exp \left(\frac{-\alpha_c F \eta}{RT} \right) \right). \quad [15]$$

Battery over potential η is defined as the difference between actual battery potentials and thermodynamic equilibrium potential U_i , as shown below:

$$\eta = \phi_s - \phi_l - U_i. \quad [16]$$

Moreover, exchange current density (i_0) connects lithium-ion concentration in electrode and electrolyte phases, and is defined using the following expression:

$$i_0 = F(k_c)^{\alpha_a} (k_a)^{\alpha_c} (c_{s,max} - c_s)^{\alpha_a} (c_s)^{\alpha_c} (c_l/c_{l,ref})^{\alpha_a}. \quad [17]$$

Here, k represents temperature dependent reaction rate (subscripts a and c represent anode and cathode respectively).

Energy balance.—During a charge-discharge cycle, heat is readily generated in battery. Many parameters such as diffusivity, reaction constant, conductivity, thermodynamic potential and activity are temperature dependent variables. Therefore, for monitoring temperature variations a heat model is coupled with the above mentioned battery model. The heat source is broadly classified into three parts: reversible

heat, Ohmic heat and active polarization heat.²² Overall, heat equation can be written as:

$$\rho_i c_{p,i} \frac{\partial T}{\partial t} + \nabla \cdot (-k_i^{th} \nabla T) = (Q_{rev} + Q_{act} + Q_{ohm}), \quad [18]$$

where, reversible, Ohmic and active polarization heats are:

$$Q_{rev} = a_{v,i} i_{loc,i} T \frac{\partial U_i}{\partial T}. \quad [19]$$

$$Q_{ohm} = \sigma_{s,eff} \nabla \phi_s \cdot \nabla \phi_s + \sigma_{l,eff} \nabla \phi_l \cdot \nabla \phi_l + \kappa_D^{eff} \frac{\nabla c_l}{c_l} \cdot \nabla \phi_l, \quad [20]$$

where,

$$\kappa_D^{eff} = \frac{2RT}{F} \sigma_{l,eff} (t_+ - 1) (1 + d \ln f / d \ln c_l), \quad [21]$$

$$Q_{act} = a_{v,i} i_{loc,i} (\phi_{s,i} - \phi_{l,i} - U_i). \quad [22]$$

The reversible heat is generated due to change in potential with respect to change in temperature. It is termed reversible because heat loss or gain is recovered if the system is brought back to initial conditions. The Ohmic heat is generated due to charge flow through resistance. Finally, the active polarization heat is generated during reduction or oxidation of lithium-ions on electrode surface. Among different heat generation components Ohmic heat is identified as dominant component.²⁵

For boundary conditions, except boundaries 1 and 4 all other external boundaries are considered to be adiabatic. Further, boundaries 1 and 4 follow Newton's cooling law and represented as

$$\begin{aligned} -k_i^{th} \frac{\partial T}{\partial x} \Big|_{x=0} &= h(T_{amb} - T), \text{ and } -k_i^{th} \frac{\partial T}{\partial x} \Big|_{x=L_a+L_s+L_c} \\ &= h(T_{amb} - T). \end{aligned} \quad [23]$$

Where, k_i^{th} , h and T_{amb} is conductive heat transfer coefficient, lumped heat transfer coefficient and ambient temperature, respectively.

Stress model.—The paper focuses on two types of stress generation, thermal and intercalation, discussed in this section.

Thermal strain ($\varepsilon_{thermal}$) is obtained by calculating temperature difference between initial and instant temperature values with expansion coefficient value (α) of electrode materials (Eq. 24).

$$\varepsilon_{thermal} = \alpha_i \Delta T. \quad [24]$$

Previous work on intercalation stress model²⁴ discussed the governing equations related to intercalation stress and illustrates them through numerical derivations. Analogous to the model mentioned in Zhang et al.,^{24,25} stress-strain relation including concentration gradient can be written as

$$\varepsilon_{ij} = \frac{1}{E} [(1 + \vartheta) \tau_{ij} - \vartheta \tau_{kk} \delta_{ij}] + \frac{\tilde{c} \Omega}{3} \delta_{ij}, \quad [25]$$

where \tilde{c} , ϑ , and E represent concentration change from initial values, Poisson's ratio and Young modulus, respectively. For the case of spherical particle, stress tensor contains radial and tangential components. The equilibrium equation for this case can be simplified as

$$\frac{d\tau_r}{dr} + \frac{2}{r} (\tau_r - \tau_t) = 0, \quad [26]$$

and the stress-strain relations are

$$\varepsilon_r = \frac{1}{E} (\tau_r - 2\vartheta \tau_t) + \frac{\Omega}{3} \tilde{c}, \quad [27]$$

$$\varepsilon_t = \frac{1}{E} [(\tau_t - \vartheta(\tau_r + \tau_t))] + \frac{\Omega}{3} \tilde{c}. \quad [28]$$

Where, τ_r and τ_t values are described as

$$\tau_r = \frac{2\Omega E}{3(1 - \vartheta)} \left(\frac{1}{r_0^3} \int_0^{r_0} \tilde{c} r^2 dr - \frac{1}{r^3} \int_0^r \tilde{c} r^2 dr \right), \text{ and} \quad [29]$$

$$\tau_r = \frac{\Omega E}{3(1-\nu)} \left(\frac{2}{r_0^3} \int_0^{r_0} \tilde{c} r^2 dr - \frac{1}{r^3} \int_0^r \tilde{c} r^2 dr - \tilde{c} \right). \quad [30]$$

Further using Eq. 26 hydrostatic stress, τ_h , is calculated using

$$\tau_h = (\tau_r + 2\tau_t)/3. \quad [31]$$

Model Parameters and Simulation Details

Atomistic model.— The MD simulations, for anode and cathode material, are performed using both *NVT* and *NPT* ensembles. For *NVT* ensemble, the number of particles N , the volume V , and the temperature T are kept constant. For *NPT* ensemble, the number of particles N , the pressure P , and the temperature T are kept constant. Nosé-Hoover thermostat and barostat are used to maintain system temperature and pressure of the system, respectively. Periodic boundary conditions are imposed in all the spatial directions for both anode and cathode system. All simulations are performed using the LAMMPS⁴⁴ with a time step of 0.1 fs, and a cut off distance, for all interactions, is fixed at 12 Å.

Macro model.— Table I list different parameters for lithium based rechargeable batteries. The parameters include values related to design specifications, lithium concentration, heat transfer, intercalation stress calculation, kinetic and transport properties. In order to simulate the battery charge-discharge process, a charge-discharge square pulse, with a time constant of 800 s each, is applied with current density (I_{app}) of 17.5 Am⁻² at boundary 4 (see Fig. 1).

Electrode properties.— Open circuit voltage (OCV) for both positive electrode (U_p) and negative electrode (U_n) comes from Doyle et al.²⁰ Whereas, entropy change in electrode $\Delta S_i = dU_i/dT$, is adopted from Ye et al.²³ Further, state of charge (SOC), given by Eq. 32, is used as a parameter in measuring OCV and entropy change.

$$SOC = \frac{C_{s,0}}{C_{s,max}} \quad [32]$$

The macro simulations are performed using COMSOL Multiphysics software. The complete battery setup, described in Fig. 1, is considered as a combination of 1D battery model and 2D electrode particle model. The 1D model contains 16 edge elements (mesh length-33.5 mm) and the 2D model contains 162 and 126 triangular elements for anode and cathode, respectively. The governing equations described in section 2.2 are represented using a combination of battery module, heat module and PDE module available in COMSOL.

Results and Discussion

We start the lithium-ion diffusion behavior for both anode and cathode. Fig. 2a shows the MSD curve for different concentration of lithium in graphite. The corresponding diffusivity values evaluated as per Eq. 3 are plotted in Fig. 2b. The

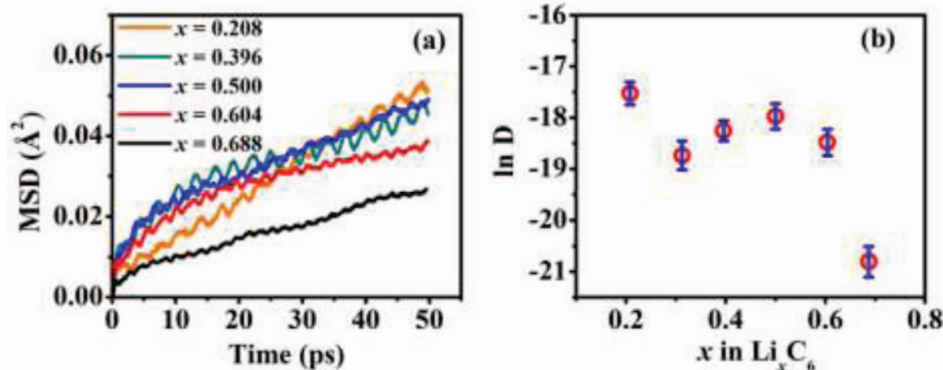


Figure 2. (a) MSD vs. time plot for various Li ion concentration, (b) diffusivity (in cm² s⁻¹) as a function of Li ion concentration. Error in the diffusivity value (from block average) is typically ~10%.

Table I. Design specifications associated modeling parameters.

	Anode	Separator	Cathode	Ref.
<i>Design Specifications</i>				
ϵ_l	0.357	1	0.444	20
ϵ_s	0.471		0.297	20
L_i (μm)	100	52	183	Assumed
R_i (μm)	12.5		8	Assumed
<i>Lithium ion concentrations</i>				
$C_{s,0}$ (mol m ⁻³)	14870		3900	20
$C_{s,max}$ (mol m ⁻³)	26390		22860	20
$SOC_{0,i}$	0.563		0.17	Calculated
<i>Kinetic and Transport Properties</i>				
$\alpha_{a,i}, \alpha_{c,i}$	0.5		0.5	20
γ_i	1.5	1.5	1.5	20
D_i (cm ² s ⁻¹)	7.5×10^{-11}	7.5×10^{-11}	7.5×10^{-11}	20
$E_{a,D,i}$ (kJ mol ⁻¹)	7.86		17	Calculated
k_i (m/s)	2×10^{-11}		2×10^{-11}	20
σ_s (S/m)	100		3.8	20
t^+	0.363	0.363	0.363	20
<i>Thermal Properties</i>				
k_i^{th} (W m ⁻¹ K ⁻¹)	1.7	0.16	2.1	21,22
ρ_i (kg m ⁻³)	5031.67	1500	2292	21,22
$C_{p,i}$ (J Kg ⁻¹ K ⁻¹)	700	700	700	21,22
T_{ref} (K)	298	298	298	Assumed
<i>Intercalation Stress Properties</i>				
E (GPa)	12		10	54
ν	0.3		0.3	54
Ω (m ³ mol ⁻¹)	4.17×10^{-6}		3.5×10^{-6}	54

lithium-ion diffusivity in graphite at a constant temperature evaluated in this paper is compared with earlier findings of Persson et al.,^{15,34} obtained from first principles calculation. The Li_xC₆ model used in this work is an AB hexagonal stacking (for $0 < x < 1$), and differs from the model used in Persson et al.,¹⁵ which is a combination of AABB stacking ($0 < x < 0.5$) and AB ($0.5 < x < 1$) stacking. However, the nature of the diffusivity curve obtained in this work is in line with their findings. For $x > 0.5$, there is a decrease in the diffusivity value with increasing x . This decreasing trend can be attributed to the repulsive lithium-lithium interaction due to increasing lithium-ion concentration. The range of diffusivity is within the numerical limits given in Persson et al.³⁴ It should be noted that MD simulation used here indicates hopping based mechanism with periodic discontinuity. The obtained results are in good agreement with the quantum mechanics (QM) values presented in the work of Persson et al.^{15,34} The coherence between these two results shows the effectiveness of the atomistic simulations in determining diffusivity value for graphite anode. To derive a temperature dependence of diffusivity presented in Eq. 4, molecular dynamics simulations are performed for the anode, at a constant lithium-ion concentration, for varying temperature. Typical MSD curve at $x = 0.369$ is shown in

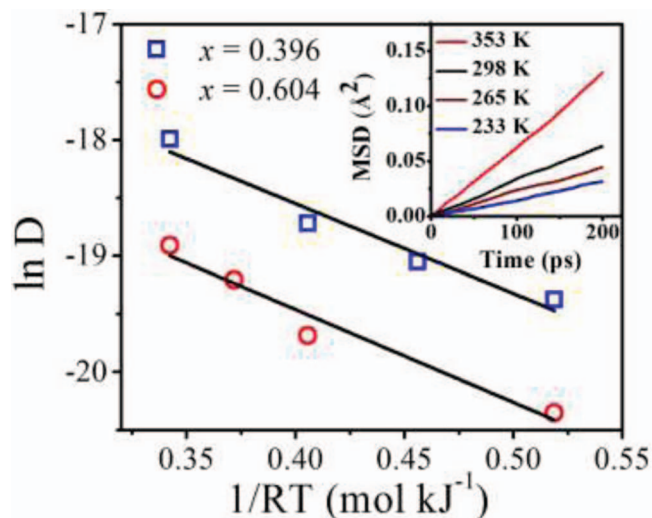


Figure 3. Arrhenius plot for different concentration of x in Li_xC_6 . The inset is MSD vs. time plot for ($x = 0.396$) at different temperatures. Unit of diffusivity used in y axis is $\text{cm}^2 \text{s}^{-1}$.

Fig. 3 (inset) as an illustration. An Arrhenius plot obtained for different concentration values of lithium-ions is shown in Fig. 3, and is used to estimate the activation energy. The estimated activation energy is in agreement with the values obtained from experiments³⁵ (5.1 kJ/mol at 0% SOC) and quantum simulation⁴⁵ (4.51 kJ/mol). Finally, an average of activation energy of 7.86 kJ/mol as per Fig. 3 is used for finite element simulation.

In order to understand the effect of lithium-ion concentration and temperature on diffusivity of lithium ion in electrodes, we also calculated the stress generated during lithium-ion intercalation in graphite electrode of lithium-ion batteries. The average compressive stress of Li_xC_6 anode at 298 K, using *NVT* simulation, is found to be 24.7 GPa and 8.4 GPa for $x = 0.369$ and 0.604, respectively; while at high temperature (325 K), the corresponding stress values are 38.9 GPa and 8.2 GPa, respectively. At low lithium-ion concentration ($x = 0.369$), stress increase with an increase in temperature. On the other hand, at high concentration ($x = 0.604$) stress decreases with increase in temperature. This is clearly related to the diffusivity behavior seen earlier, which has an opposite behavior at low and high concentration, akin to the behavior seen for the compressive stress. Hence, it is evident that the compressive stress in the system directly influences the diffusivity at different lithium-ion concentration and temperature in Li_xC_6 .

We have undertaken a similar approach for cathode material, LiMn_2O_4 , and molecular simulations are performed for different temperatures and lithium-ion concentration. The MSD of lithium-ions at various temperatures is similar to that seen for other cathode materials such as LiFePO_4 , having similar characteristics of diffusion.⁴⁶ The diffusivity values are calculated using the Einstein relation (Eq. 3) based on the different MSD curves generated for various lithium-ion concentrations. A diffusivity data is presented in Fig. 4 to show the variation in diffusivity with lithium-ion concentration at 300 K. Lithium ions prefers to be within the hexagon lattice of the graphene sheets. At a low concentration, ion moves due to the hopping mechanism. As the ion concentration increase, in general, the hexagonal rings get saturated which reduces the mobility or diffusivity of the lithium ions. The diffusivity value at lower concentrations is larger than that at higher concentrations. Fig. 5 summarizes the behavior of diffusivity as a function of temperature for two concentrations viz., 0.7 and 1.0. The diffusivity value shows an increasing trend with temperature. The activation energy at each concentration can be obtained by taking the slope of linear behavior of diffusivity against temperature. In this work, average activation energy of 17 kJ/mol is used based on Fig. 5. This estimation is in line with activation energy reported in literature.²² The concentration and temperature variation

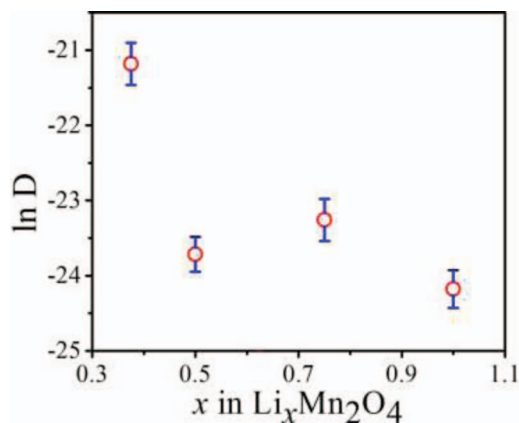


Figure 4. $\text{Li}_x\text{Mn}_2\text{O}_4$ diffusivity (in $\text{cm}^2 \text{s}^{-1}$) as a function of Li-ion concentration at $T = 300 \text{ K}$.

terms combined together forms the Arrhenius expression (Eq. 4) for diffusivity.

To this end, we utilize the diffusivity expression generated from atomistic simulation in the macro modeling equations as described in section 2. A normalized battery potential plot is developed and presented in Fig. 6, where maximum battery potential is used for the normalization. Fig. 6 shows the deteriorating battery potential/cell performance with time. After a total of 100 charge-discharge cycles a drop of around 10% in the peak battery potential is seen. Moreover, decline in the potential is higher during the initial period, and it decreases in later cycles. The decline is mainly attributed to the accumulation of intercalation stress. However, performance is also hampered by the development of concentration gradient. Fig. 7a presents a plot of concentration gradient in the electrolyte medium, generated for the discharging period. A continuous development of concentration gradient is clearly evident from the plot. During an electrochemical process, lithium-ions are continuously produced at the negative electrode and consumed at the positive electrode. The imbalance between production and consumption of lithium-ions at negative and positive electrode surfaces give rise to the concentration gradient. The gradient tends to increase with time resulting in decline of current density. Transport properties like electrical conductivity, transference number of lithium-ions and diffusion coefficient of lithium-ions in electrolyte polymer are concentration dependent.²⁰ Therefore, concentration gradient can also acts as a promoter to the capacity fade problem with each cycle, adversely affecting the battery performance. Due to these possible effects we consider concentrated solution theory, for battery

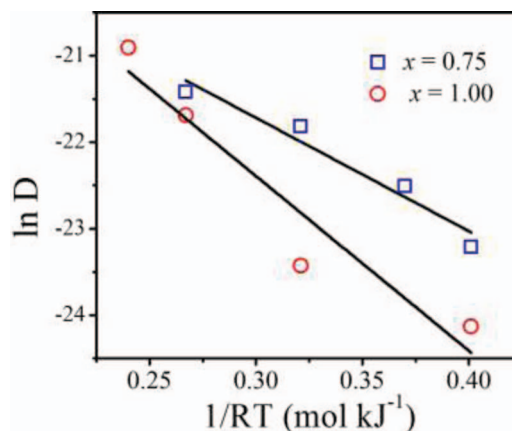


Figure 5. Li-ion diffusivity (in $\text{cm}^2 \text{s}^{-1}$) as a function of temperature at $x = 1$ and $x = 0.75$.

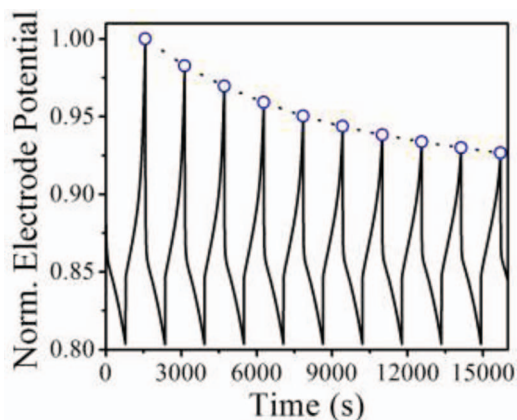


Figure 6. Normalized potential (peak stress value during simulation is used for normalizing) for charge-discharge cycles.

electrolytes, for the development of a rigorous model. As a resultant of concentration gradient the absolute value of electrolyte potential starts increasing as shown in Fig. 7b. A reverse trend in concentration gradient is seen for the charging phase, because of the swap of role between positive and negative electrodes.

Thermal management is one of the key issues in lithium-ion battery from both safety and performance point of view. Lithium-ion battery poses the threat of thermal runaway due to thermal abuse,^{5,47} which possibly could also be due to high intercalation stress at high temperature.²⁵ Hence, understanding and monitoring thermal behavior of lithium-ion battery is extremely important. In this work, total heat generated in the system is uniformly distributed for calculating battery temperature. Also, as mentioned in the model assumptions, there is no temperature gradient assumed in the electrode particle. Fig. 8 presents a battery temperature behavior for the model as a function of charge-discharge cycle. In the initial part, battery temperature increases because of the heat generation. However, due to the counterbalancing heat removal system the rate of increase in temperatures slows down. This results in battery temperature to approach an asymptotic value. The current simulation does not involve any abrupt changes i.e. the temperature rise stays within the allowable limit: 85–120°C.⁴⁸

In addition to the safety aspect of batteries, capacity fade also becomes a concern due to enhanced temperature during the charge-discharge cycle. At an elevated temperature, anode (graphite) SEI (solid-electrolyte interface) can get damaged inducing capacity fade problem.⁴⁹ This is because of an intrinsic volume change, which occurs in graphite electrode particle at high temperature, and anode elasticity is not sufficient to accommodate such volume changes.⁵⁰ Hence, it is important to design battery model that avoids high temperature rise.

As stated earlier, one of the predominant causes of capacity fade problem and subsequently decline in the performance is the accumulation of intercalation stress.^{24–32} Intercalation stress can affect

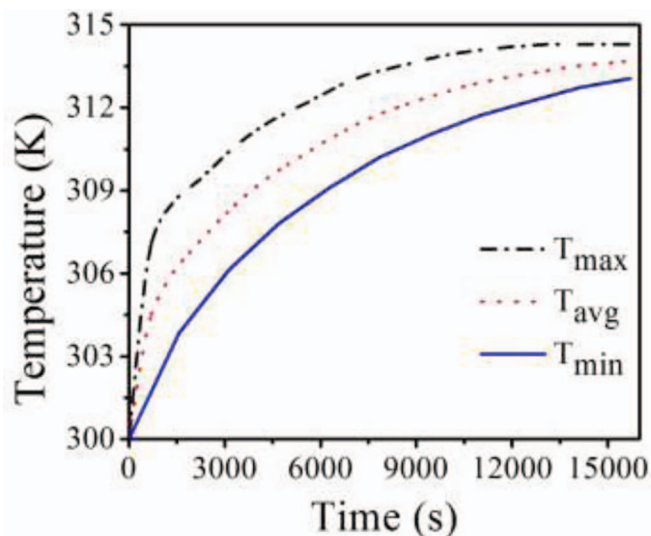


Figure 8. Maxima, minima and average temperature profile for the Li-ion battery for 10 charge-discharge cycles.

the electrode particles in several ways, mainly inducing large volume change in electrode particles that may lead to nucleation and growth of cracks.^{27,28,30,32} This consequently leads to degradation of active electrode materials and therefore promulgating capacity fade problem.^{27,30} In this work, the stress at particle radius for both cathode and anode is found oscillatory in nature as shown in Fig. 9a. This is due to the applied periodic charge-discharge cycle. Recently, Cannarella et al.⁵¹ have shown the stress present in battery stack as a dynamic quantity, fluctuating with charge-discharge cycle, which increases irreversibly over the course of time. In this paper, we have shown that as the cycle progress the maximum stress tends to increase indicating an accumulation of the stress in the system. The peak stress values, if joined by a curve, clearly indicate an increasing trend in case of anode. This confirms accumulation of stress with time. However, the increasing trend is not significant in case of cathode. The disparity can be mainly attributed to the diffusivity values, which is higher for anode compared to that for cathode. Hence, it is apparent that high diffusivity values induce higher intercalation stress. In order to show the accumulation of stress more coherently, peak tangential stress values are calculated at the anode center for 100 cycles (Fig. 9b). For the corresponding time cathode tangential stress values are also calculated at the cathode center. The obtained results show a clear growth in the stress values with battery usage. This accumulating stress not only hampers the battery performance as shown in Fig. 6, but may even lead to electrode cracking, and hence complete break down if stress generated in electrode material exceeds the limit. This is also suggested by the stress generation and electrode cracking model of Christensen et al.²⁶ All other intercalation stress components follow similar nature as in Fig. 9a. In order to relate deteriorating battery performance and successive accumulation of stress, tangential stresses at particle surface for anode and cathode are plotted with respect to time corresponding to the peak electrode potential during charge-discharge cycles, and is shown in Fig. 10. Electrode potential and stress values are considered in the normalized form, where a maximum of respective parameters are used for normalization. It shows accumulation of stress (particular at the anode) is directly related to the decline in battery potential, as evident from Fig. 10.

To understand the effect of modified diffusivity equation on intercalation stress, two sets of simulation are performed for 100 cycles. In set 1, diffusivity expression is taken as a function of temperature and concentration adopted from atomistic simulations, developed in this paper. In simulation set 2, diffusivity is taken only as a function of temperature adopted from Doyle et al.²⁰ For both the cases all the other simulation parameters are kept identical. Fig. 11 presents

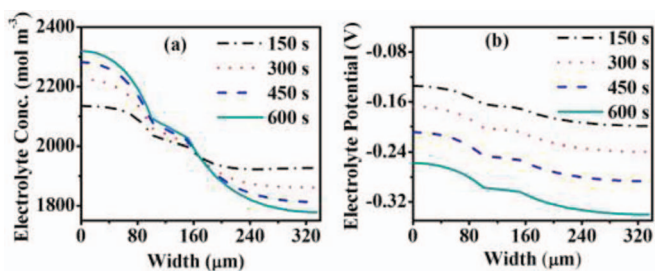


Figure 7. (a) Electrolyte concentration at different time instants during discharging period, (b) electrolyte potential at different time instants during discharging period.

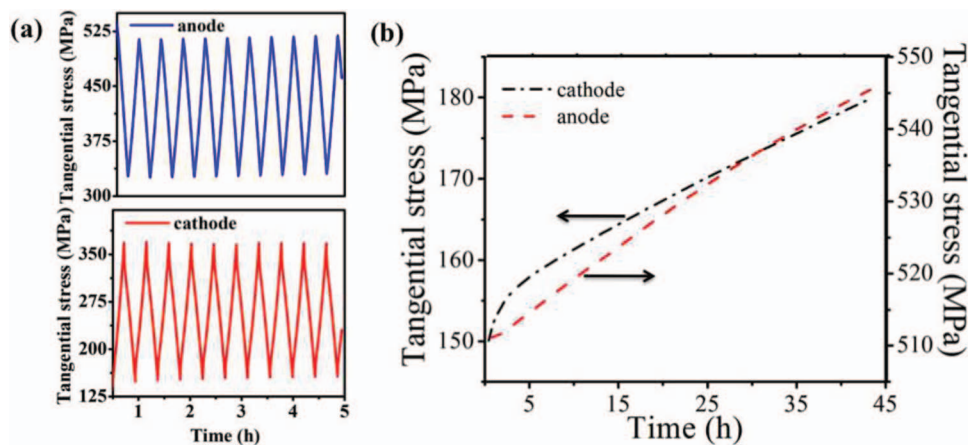


Figure 9. Panel (a) shows the tangential stress for the anode and the cathode calculated at the center of electrode particle (10 cycles). Panel (b) gives the peak tangential stress values calculated at the center of the anode and cathode as a function of time.

a comparison of radial stress (computed at particle center) for both the anode and the cathode for the above given simulation sets at two different time instants. It is evident from the figure that intercalation stress depends not only on temperature but also on lithium-ion concentration, which is more prominent in the case of anode. To make comprehensive analysis of diffusivity in electrodes, the difference between radial stresses for both the simulation sets are calculated, and is presented in Fig. 12. An oscillatory nature is visible due to applied periodic charge-discharge cycle. It can be inferred from the magnitude of difference in radial stress, for both the simulation sets, that the intercalation stress differs significantly, substantiating our earlier results. Further, the peak difference in stress is of similar order for the anode and an order lower for the cathode as compared to the actual stress. It signifies that the difference is more in case of the anode than that in the cathode. These results are in line with a recent work of Joglekar et al.^{52,53} An offset in peak values of radial stress difference with charge-discharge cycle is also observed in Fig. 12. The offset can be explained based on the electrode diffusivity and changing lithium-ion concentration. At the start of each charge-discharge cycle due to reasons involving capacity loss, the concentration of lithium-ion changes in electrode particles. Consequently, the electrode diffusivity (dependent on lithium-ion concentration as in simulation set 1) will be different for varying lithium-ion concentration, and therefore the stress, which is dependent on both diffusivity coefficient and lithium-ion concentration, will vary producing an offset. This substantiates the assertion made earlier that intercalation stress depends significantly on the lithium-ion dependent diffusivity expression. Further, it presses the need to implement lithium-ion dependent diffusivity

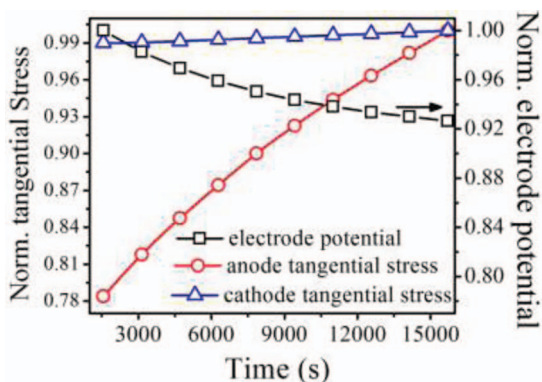


Figure 10. Comparison of decreasing peak potential with increasing anode and cathode tangential stress during charge-discharge cycle.

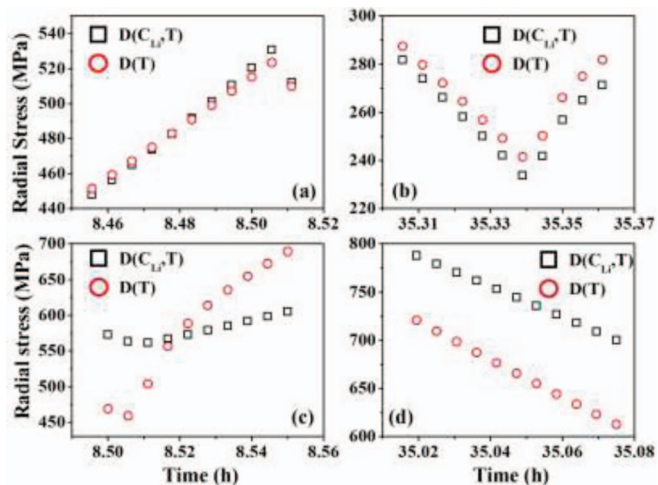


Figure 11. Radial stress computed at the center of electrode particle with respect to diffusivity (function of both concentration (C_{Li}) and temperature (T); and function of temperature (T) at two different time instants: a and b for cathode; and c and d for anode.

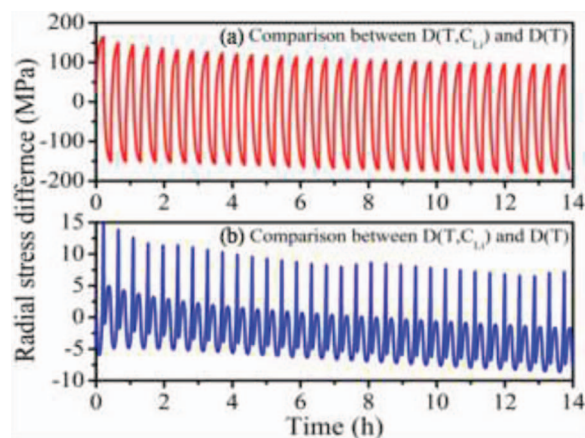


Figure 12. Comparison of radial stress difference for two different diffusivity expression for anode (a) and cathode (b); one dependent on temperature and Li-ion concentration (developed in this work) and other only on temperature (Doyle et al.²⁰).

expression for more precise prediction of battery performance, owing to its importance.

Conclusions

In this work a multi-scale battery model is developed to predict health of the battery. In the first stage diffusivity expressions are developed, using classical molecular dynamics approach, as a function of temperature and lithium-ion concentration using atomistic modeling, for both anode and cathode materials. A classical molecular dynamics approach is adopted for evaluating diffusivity expression similar to the Arrhenius expression. The diffusivity values are used in a FEM model (heat and stress model coupled together) to predict the health of the battery. It is shown that the decline in performance (~10% in 100 cycles) is directly related to the accumulation of the intercalation stress. A coupled heat model with intercalation stress model depicts that for uniform usage and proficient heat transfer values battery temperature tends to an asymptotic value. In addition, we have demonstrated the effect of electrolyte concentration gradient, electrolyte potential and over-potential on the decline in current density.

Finally, we have demonstrated that the stress values get significantly affected with the inclusion of lithium-ion concentration and temperature dependent diffusion values compared to the case of constant diffusion. The order of difference is comparable to the order of the actual stress value (for 100 cycles), clearly suggesting the need for exercising concentration and temperature dependent diffusivity equation for more accurate analysis of battery performance.

Acknowledgment

This work is supported by the Department of Science and Technology (DST), India.

References

1. A. R. Armstrong and P. G. Bruce, *Nature*, **381**, 499 (1996).
2. J.-M. Tarascon and M. Armand, *Nature*, **414**, 359 (2001).
3. H. Song, Z. Cao, X. Chen, H. Lu, M. Jia, Z. Zhang, Y. Lai, J. Li, and Y. Liu, *J. Solid State Electrochem.*, **17**, 599 (2013).
4. R. Premanand, A. Durairajan, B. Haran, R. White, and B. Popov, *J. Electrochem. Soc.*, **149**, A54 (2002).
5. G.-H. Kim, A. Pesaran, and R. Spotnitz, *J. Power Sources*, **170**, 476 (2007).
6. D. Aurbach, Y. Talyosef, B. Markovsky, E. Markevich, E. Zinigrad, L. Asraf, J. S. Gnanaraj, and H.-J. Kim, *Electrochim. Acta*, **50**, 247 (2004).
7. S. S. Zhang, *J. Power Sources*, **162**, 1379 (2006).
8. S.-Y. Chung, J. T. Bloking, and Y.-M. Chiang, *Nat. Mater.*, **1**, 123 (2002).
9. B. J. Landi, C. D. Cress, and R. P. Raffaele, *J. Mater. Res.*, **25**, 1636 (2010).
10. M. C. Tucker, J. A. Reimer, and E. J. Cairns, *J. Electrochem. Soc.*, **149**, A574 (2002).
11. Q.-C. Zhuang, T. Wei, L.-L. Du, Y.-L. Cui, L. Fang, and S.-G. Sun, *J. Phys. Chem. C*, **114**, 8614 (2010).
12. K. W. Nam, W.-S. Yoon, H. Shin, K. Y. Chung, S. Choi, and X.-Q. Yang, *J. Power Sources*, **192**, 652 (2009).
13. J. Li, E. Murphy, J. Winnick, and P. A. Kohl, *J. Power Sources*, **102**, 294 (2001).
14. G. Ceder, Y. M. Chiang, D. R. Sadoway, M. K. Aydinol, Y. I. Jang, and B. Huang, *Nature*, **32**, 694 (1998).
15. K. Persson, Y. Hinuma, Y. S. Meng, A. V. der Ven, and G. Ceder, *Phys. Rev. B*, **82**, 125416 (2010).
16. K. Tateishi, D. d. Boulay, and N. Ishizawa, *Appl. Phys. Lett.*, **84**, 529 (2004).
17. K. Tateishi, D. d. Boulay, N. Ishizawa, and K. Kawamura, *J. Solid State Chem.*, **174**, 175 (2003).
18. I. Y. Gotlib, I. V. Murin, and E. M. Piotrovskaya, *Inorg. Mater.*, **39**, 404 (2003).
19. E. Martínez-Rosas, R. Vasquez-Medrano, and A. Flores-Tlacuahuac, *Comput. Chem. Eng.*, **35**, 1937 (2011).
20. M. Doyle and J. Newman, *J. Electrochem. Soc.*, **143**, 1890 (1996).
21. K. Kumaresan, G. Sikha, and R. E. White, *J. Electrochem. Soc.*, **155**, A164 (2008).
22. V. Srinivasan and C. Y. Wang, *J. Electrochem. Soc.*, **150**, A98 (2003).
23. Y. Ye, Y. Shi, N. Cai, J. Lee, and X. He, *J. Power Sources*, **199**, 227 (2012).
24. X. Zhang, W. Shyy, and A. M. Sastry, *J. Electrochem. Soc.*, **154**, A910 (2007).
25. X. Zhang, A. M. Sastry, and W. Shyy, *J. Electrochem. Soc.*, **155**, A542 (2008).
26. J. Christensen and J. Newman, *J. Electrochem. Soc.*, **153**, A1019 (2006).
27. W. H. Woodford, Y.-M. Chiang, and W. C. Carter, *J. Electrochem. Soc.*, **A1052** (2010).
28. J. Christensen, *J. Electrochem. Soc.*, **157**, A366 (2010).
29. Y.-T. Cheng and M. W. Verbrugge, *J. Appl. Phys.*, **104**, 083521 (2008).
30. R. Deshpande, Y.-T. Cheng, and M. W. Verbrugge, *J. Power Sources*, **195**, 5081 (2010).
31. M. W. Verbrugge and Y.-T. Cheng, *J. Electrochem. Soc.*, **156**, A927 (2009).
32. Y.-T. Cheng and M. W. Verbrugge, *J. Power Sources*, **190**, 453 (2009).
33. A. Márquez, A. Vergas, and P. B. Balbeuna, *J. Electrochem. Soc.*, **145**, 3328 (1998).
34. K. Persson, V. A. Sethuraman, L. J. Hardwick, Y. Hinuma, Y. S. Meng, A. v. d. Ven, V. Srinivasan, R. Kostecki, and G. Ceder, *Phys. Chem. Lett.*, **1**, 1176 (2010).
35. P. Yu, B. N. Popov, J. A. Ritter, and R. E. White, *J. Electrochem. Soc.*, **146**, 8 (1999).
36. Q. Wang, H. Li, X. Huang, and L. Chen, *J. Electrochem. Soc.*, **148**, A737 (2001).
37. M. Nishizawa, R. Hashitani, T. Itoh, T. Matsue, and I. Uchida, *Electrochem. Solid-State Lett.*, **1**, 10 (1998).
38. C. Y. Ouyang, S. Q. Shi, Z. X. Wang, H. Li, X. J. Huang, and L. Q. Chen, *Europhys. Lett.*, **67**, 28 (2004).
39. S. J. Stuart, A. B. Tutein, and J. A. Harrison, *J. Chem. Phys.*, **112**, 6472 (2000).
40. M. C. F. Wander and K. L. Shuford, *J. Phys. Chem. C*, **115**, 23610 (2011).
41. M. Tachibana, T. Tojo, H. Kawaji, T. Atake, N. Morita, H. Ikuta, Y. Uchimoto, and M. Wakihara, *J. Therm. Anal. Calorim.*, **69**, 997 (2002).
42. M. Gateshki, S. Hwang, D. H. Park, Y. Ren, and V. Petkov, *J. Phys. Chem. B*, **108**, 14956 (2004).
43. J. Newman and K. E. T. Alyea, *Electrochemical Systems*, John Wiley & Sons New Jersey (2004).
44. S. Plimpton, *J. Comp. Phys.*, **117**, 1 (1995).
45. H. Tachikawa and A. Shimizu, *J. Phys. Chem. B*, **110**, 20445 (2006).
46. P. Zhang, Y. Wu, D. Zhang, Q. Xu, J. Liu, X. Ren, Z. Luo, M. Wang, and W. Hong, *J. Phys. Chem. A*, **112**, 5406 (2008).
47. K. E. Thomas and J. Newman, *J. Electrochem. Soc.*, **150**, A176 (2003).
48. X.-Q. Wang, C. Yap, and A. S. Mujumdar, *Int. J. Therm. Sci.*, **47**, 1055 (2008).
49. R. Spotnitz, *J. Power Sources*, **133**, 72 (2003).
50. P. Liu, J. Wang, J. Hicks-garner, E. Sherman, S. Soukiazian, M. Verbrugge, H. Tataria, J. Musser, and P. Finamore, *J. Electrochem. Soc.*, **157**, A499 (2010).
51. J. Cannarella and C. B. Arnold, *J. Power Sources*, **245**, 745 (2014).
52. M. M. Joglekar and N. Ramakrishnan, *J. Power Sources*, **230**, 143 (2013).
53. R. Narayanrao, M. M. Joglekar, and S. Inguva, *J. Electrochem. Soc.*, **160**, A1 (2013).
54. X. Xiao, W. Wu, and X. Huang, *J. Power Sources*, **195**, 7649 (2010).